Transition-State Spectroscopy Using Ultrashort Laser Pulses

TAKAYOSHI KOBAYASHI,[1,2,3,4]* ATSUSHI YABUSHITA[3]
[1]Department of Applied Physics and Chemistry and Institute for Laser Science, University of Electro-Communications, 1-5-1 Chofugaoka, Chofu, Tokyo, 182-8585, Japan
[2]International Cooperative Research Project (ICORP), Japan Science and Technology Agency, 4-1-8 Honcho, Kawaguchi, Saitama 332-0012, Japan
[3]Department of Electrophysics, National Chiao Tung University, Hsinchu 30010, Taiwan
[4]Institute of Laser Engineering, Osaka University, 2-6 Yamada-oka, Suita, Osaka 565-0871, Japan
Phone: +81-42-443-5845
Fax: +81-42-443-5825
Email: kobayashi@ils.uec.ac.jp

Received 14 July 2010

ABSTRACT: To gain a complete understanding of a chemical reaction, it is necessary to determine the structural changes that occur to the reacting molecules during the reaction. Chemists have long dreamed of being able to determine the molecular structure changes that occur during a chemical reaction, including the structures of transition states (TSs). The use of ultrafast spectroscopy to gain a detailed knowledge of chemical reactions (including their TSs) promises to be a revolutionary way to increase reaction efficiencies and enhance the reaction products, which is difficult to do using conventional methods that are based on trial and error. To confirm the molecular structures of TSs predicted by theoretical analysis, chemists have long desired to directly observe the TSs of chemical reactions. Direct observations have been realized by ultrafast spectroscopy using ultrashort laser pulses. Our group has been able to stably generate visible to near-infrared sub-5-fs laser pulses using a noncollinear optical parametric amplifier (NOPA). We used these sub-5-fs pulses to study reaction processes (including their TSs) by detecting structural changes. We determine reaction mechanisms by observing the TSs in a chemical reaction and by performing density-functional theory calculations. **DOI 10.1002/tcr.201000018**

Key words: lasers, reaction dynamics, transition states, ultrafast spectroscopy

Introduction

Chemists have long dreamed of being able to trace chemical reaction paths by determining the structures of intermediates, including transition states (TSs). Studies in physical chemistry have recently succeeded in identifying reaction intermediates. In addition, theoretical analysis can be used to investigate TSs. The use of ultrafast spectroscopy to gain a detailed knowledge of chemical reactions (including their TSs) promises to be a progressive way to increase reaction efficiencies and enhance the reaction products, which is difficult to do using conventional methods that are based on trial and error. To confirm the

molecular structures of TSs predicted by theoretical analysis, chemists have long desired to directly observe the TSs of chemical reactions.

Transient intermediate species in photoisomerization can be revealed by ultrafast laser spectroscopy using ultrashort laser pulses, as has been performed for chemical reactions.[1,2] Ultrafast spectroscopy is complementary to the X-ray diffraction technique and electron diffraction methods. Anfinrud performed picosecond time-resolved X-ray crystallography to probe protein function in real time.[3] The electron diffraction methods were used to study an atomic-level view of the melting process of aluminum by Miller and co-workers.[4] Zewail's groups have determined dark structures in molecular radiationless transitions by ultrafast diffraction.[5]

Performing ultrafast time-resolved absorption spectroscopy using ultrashort pulses allows the vibrational amplitude to be detected with a subfemtosecond resolution owing to the short pulse duration and the high signal-to-noise ratio. Ultrafast spectroscopy offers much higher time resolutions than electron and X-ray diffraction. In addition, it can be used for measurements of amorphous materials and liquids, which are difficult to analyze by X-ray or electron diffraction. As was reported in a previous paper of ours,[6] time-resolved absorption change measurements elucidated ultrafast change in the frequencies of in-plane and out-of-plane bending modes associated with structural changes during photoisomerization and the transition state was determined.

Direct observations have been realized by ultrafast spectroscopy using ultrashort laser pulses. Using a noncollinear

Takayoshi Kobayashi was born in Niigata Prefecture in 1944. He graduated from the University of Tokyo and got his bachelor, master, and doctor degrees from the same university. He joined the Institute of Physical and Chemical Research (Riken). Between 1977 and 1979, he was a temporary member of the Technical Staff in Bell Laboratories. In 1980, he joined the Department of Physics, The University of Tokyo, as an Associate Professor and was promoted to a Full Professor in 1994. In March 2006, he was appointed as an ICORP (International Cooperative Research Project) Research Director of Ultrashort Pulse Laser Project. He then retired from the university and in April 2006 he moved to the Department of Applied Physics and Chemistry at the University of Electro-Communications, another national university in Tokyo. From April 2006, he was appointed Chair Professor of National Chiao-Tung University and the Director of the Advanced Ultrafast Laser Center. He was awarded a Scientific Achievement Award from the Chemical Society of Japan in 1995, and appointed as a Fellow of the Optical Society of America in 2000. He was awarded the Scientific Achievement Award from the Spectroscopy Society of Japan in 2003 and the Scientific Achievement Award from the Matsuo Foundation in 2005. In 2006, he received the Outstanding Science Scholar Award from Foundation for the Advancement of Outstanding Scholarship in Taiwan. He was awarded with the Outstanding Contribution to Science and Technology Award from the Shimadzu Science and Technology Foundation, Japan Minister of Education, Culture, Science Award, the Humboldt Research Award in 2010. ■

Atsushi Yabushita was born in 1976 in Osaka, Japan. He graduated from the University of Tokyo, Japan and received his BSc (1999), MSc (2001), and PhD (2004) degrees in Physics from the same university under the supervision of Professor Takayoshi Kobayashi. He is a member of the Physical Society of Japan. His research interests are in the areas of ultrafast optics, ultrafast spectroscopy, photochemistry, photobiology, and quantum information experiments. In 2004, he became a Research Associate in the Department of Physics, Faculty of Science at University of Tokyo. In 2006, he moved to Taiwan to join the Department of Electrophysics, Faculty of Science, at National Chiao-Tung University as an Assistant Professor. ■

optical parametric amplifier (NOPA),[7,8,9,10,11,12] which was developed in 2002, our group has been able to generate stable visible to near-infrared (IR) sub-5-fs laser pulses. We have used these sub-5-fs pulses to study reaction processes (including their TSs) by detecting structural changes.[13,14,15,16] This review is organized as follows. Firstly, the development of ultrashort pulse light sources is reviewed, focusing particularly on the NOPA. Following this, the principles of real-time vibrational spectroscopy are described and a comparison is given concerning how it differs from conventional vibrational spectroscopic techniques (e.g., time-resolved IR absorption and Raman spectroscopies). The next section explains how real-time vibrational spectroscopy probes the modulation of electronic transition probabilities, which reflect wave-packet motion. Examples of applications of real-time spectroscopy will immediately follow. Finally, a summary and discussion of future prospects is provided.

Development of Ultrashort Pulse Light Sources

Noncollinear Parametric Amplifier

A NOPA, the design of which is described in this paper, consists of three stages. The first stage is the parametric amplifier itself, which has a sufficiently high gain bandwidth to support sub-4-fs operation. The second stage is a grating–chirped-mirror compressor, which is used to approximately compensate for group delay. It has a flexible mirror, which is used to finely adjust the spectral phase. The third stage is used to diagnose the pulses and it is based on second-harmonic-generation (SHG) frequency-resolved optical gating (FROG) with feedback to a personal computer (which also controls the actuators of the flexible mirror). Figure 1 shows an overview of the amplifier. The system is pumped by 120-fs pulses from a regenerative amplifier (CPA1000, Clark MXR Inc.) at a repetition rate of 1 kHz. The amplifier is seeded by a fiber oscillator (Femtolite, IMRA Inc.). Below, we consider the design and function of each stage of this setup.

Extension of Phase-Matching Bandwidth

The discovery of "magic" phase-matching conditions in a type-I β-barium borate (BBO) crystal pumped by 400-nm light[17,18] opened the way to generate amplified visible pulses that have a bandwidth of nearly 200 THz.[7,19] The pumping arrangement used to achieve these phase-matching conditions is unique since the angle of the pump beam relative to the seed beam (about 3.7°) is almost exactly equal to the birefringent walk-off angle between ordinary and extraordinary waves inside the crystal. Consequently, BBO crystals as long as 1–2 mm can be employed in 5-fs NOPAs. The noncollinear

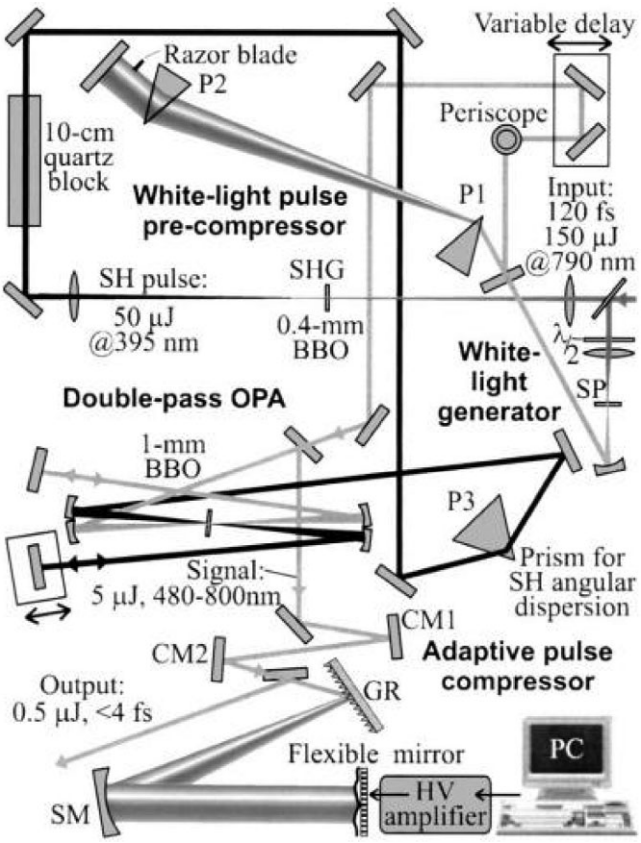

Fig. 1. Schematic of experimental setup. $\lambda/2$: −800 nm wave plate; SP: 2-mm-thick sapphire plate; P1,2: 45° quartz prisms; P3: 69° quartz prism; CM1,2: ultrabroadband chirped mirrors; GR: 300-lines/mm diffraction grating (Jobin Yvon); SM: spherical mirror, $R = -400$ mm; SHG crystal: 0.4-mm, $\theta = 29°$ BBO (Eksma); NOPA crystal, 1-mm $\theta = 31.5°$ BBO (Casix).

phase matching conditions are well understood and have been discussed in numerous studies.[7,18,19,20,21,22,23,24,25,26]

Shirakawa and co-workers have investigated the subtleties of parametric amplification using a noncollinear configuration.[25,26] They considered the effect of tilting of the signal pulse front on the ability to compress the signal pulse into a sub-5-fs pulse. They proposed using a pump beam with a tilted wavefront to prevent tilting of the signal pulse in space (which causes angular dispersion of the amplified pulse). This configuration (known as pulse-front matching) was implemented by sending the pump beam through a prism and adjusting the pulse-front tilt using a telescope consisting of two convex lenses.[27]

The angular dispersion of the pump beam of a sub-5-fs NOPA is important for increasing the phase-matching bandwidth. When considering the mechanism responsible for this broadening, it is important to remember that the pump is not monochromatic and its spectral extent is determined by the duration of the input fundamental pulses and the frequency-

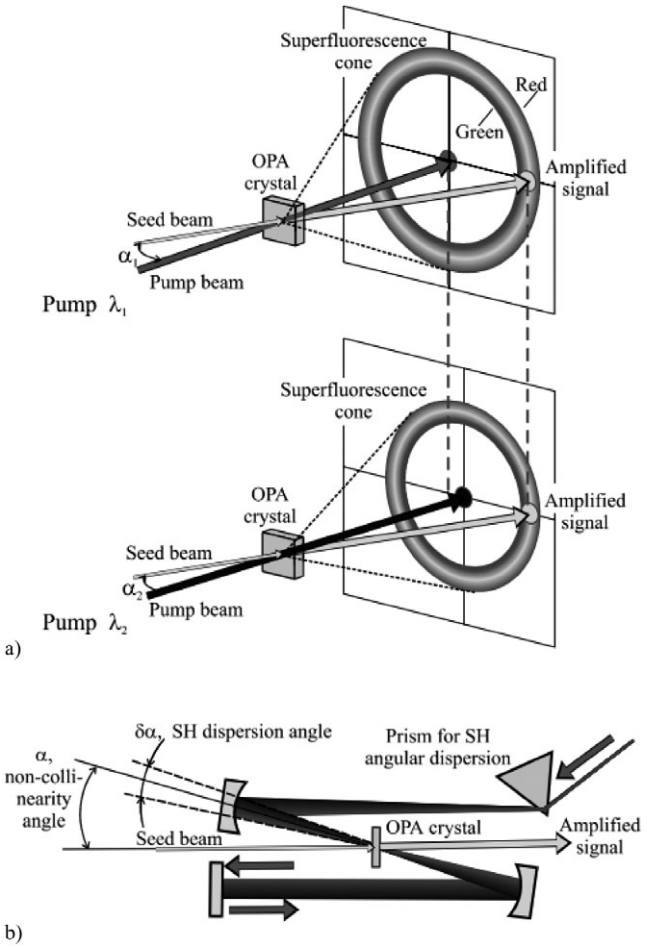

Fig. 2. Increasing the parametric bandwidth by adjusting the incidence angles of individual pump wavelengths onto the NOPA crystal. a) Schematic representation of noncollinear pumping geometry. b) SH dispersion adjustment using a prism and a focusing optic.

doubling conditions. Even with relatively thick SHG crystals (1–2 mm lithium triborate or BBO) and comparatively long (120–150 fs) pulses generated using a conventional regenerative amplifier to pump the NOPA,[7,19] the resulting second-harmonic (SH) radiation has a bandwidth of several nanometers. Figure 2 schematically depicts how this can be used to improve the phase-matching conditions.

The noncollinearity angle, α, can be optimized to minimize the solid angle over which broadband superfluorescence is emitted.

Wide-bandwidth parametric amplification can subsequently be achieved by aligning the seed beam in that direction. In other words, each pump wavelength has a different optimal noncollinearity angle α. The pump beam dispersion for phase-matching optimization is adjusted by selecting the apex angle of the prism in the SH pathway (Fig. 2b) and the distance between the prism and the focusing optic *l*. The required SH dispersion can be calculated using the simplified equation, Equation (1):

$$\delta\alpha(\lambda) = \mathrm{a\,tan}\left[\tan(\gamma(\lambda_0) - \gamma(\lambda))\frac{l}{f}\right], \qquad (1)$$

where λ is the pump (SH) wavelength, λ_0 is the central component of the SH spectrum, f is the focal distance, and $\gamma(\lambda)$ is the exit angle of the SH beam after the prism, which is given by Equation (2):

$$\gamma(\lambda) = \mathrm{a\,sin}\left[n(\lambda)\sin\left[\beta - \mathrm{a\,sin}\left(\frac{\sin\gamma_0}{n(\lambda)}\right)\right]\right], \qquad (2)$$

where γ_0 is the angle between the SH beam and the normal of the input face of the prism (i.e., the incidence angle onto the prism), β is the apex angle of the prism, and $n(\lambda)$ is the refractive index of glass.

Time Window for Broadband Parametric Amplification

To achieve ultrashort pulses, it is important to consider time-domain shaping of the amplified radiation. Despite the extremely broad bandwidth of the parametric gain, only the spectral components of the seed that temporally overlap with the pump pulse are amplified. There are two methods for increasing the time window for amplification: elongating the pump pulse or compressing the seed. Our system employs both methods.

To stretch the pump pulse, we installed a 10-cm quartz crystal in the SH beam, which is used to pump the NOPA. As a result of stretching the SH pulse, we were able to utilize a confocal focusing arrangement for the pump beam (Fig. 1), which produced a significantly cleaner mode structure of the output beam than the nonconfocal pump arrangement, which we had used in previous studies.[7,28]

The white-light seed does not require meticulous precompression to achieve the maximum bandwidth for simultaneous phase matching. In our NOPA design, the white-light continuum produced in a 2-mm-thick sapphire window passes through a pair of 45° quartz prisms that are separated from each other by ~50 cm. The prism precompressor performs three distinct functions in the system. First, by placing an adjustable razor blade behind the inner prism, we can eliminate the intense frequency components of the fundamental pulse injected into the sapphire window and prevent their undesirable amplification in the NOPA crystal. Second, the insertion depth of the inner prism determines the so-called horizon wavelength (i.e., the minimum wavelength transmitted

through the prism sequence). Finally, by balancing the dispersion of the precompressor, we can optimize the temporal window of parametric amplification and the output spectral shape.

We have demonstrated that a high level of seed precompression is not required to achieve broadband amplification. Instead, flexible spectral shaping of the amplified signal is attained by balancing the pump–seed delay for each of the two passes through the NOPA crystal.

Pulse Compressor Design

Our experimental arrangement (see Fig. 1) is based on a 300 lines/mm diffraction grating and a spherical reflector ($R = -400$ mm) with a flexible mirror positioned in the focal plane. This scheme operates in the negative dispersion regime when the −1 diffraction order of the grating is selected. Tuning the position of the membrane of the micro-machined mirror allows the group delay to be corrected in the range of 40 fs. Therefore, the main correction of the spectral phase should be performed by adjusting other elements of the pulse compressor; the computer-controlled flexible mirror can only be employed for fine-tuning the group delay.

Figure 3 presents the overall dispersive properties of the designed compressor.

In this figure, the solid circles indicate the target group delay (i.e., the chirped-pulse characterization result (Figure 4) with its sign reversed).

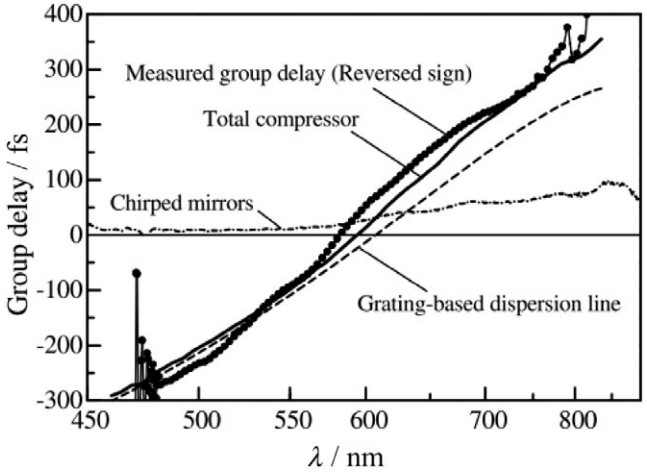

Fig. 3. Overview of compressor dispersion. The solid circles indicate the target group delay, corresponding to time-inverted data. The solid curve gives the overall group delay of the compressor, excluding the contribution of the flexible mirror. The dashed curve depicts the estimated group delay of the telescopic grating-based disperser, whereas the dash-dotted curve represents the contribution of the dielectric chirped mirrors measured by white-light interferometry.

The telescopic grating disperser (dashed curve) contributes most of the required negative dispersion. The dispersion can be tuned from positive to negative by varying the reflection angle of the spherical mirror and the distance between the mirror and the grating. However, such manipulations can easily result in spatial chirping of the output beam. We have performed a careful dispersive ray-tracing analysis of the system to determine the optimal conditions that both satisfy the group delay requirements and achieve a high spatial beam quality. To introduce additional negative dispersion that cannot be provided by the grating–mirror arrangement, we employed two dielectric ultrabroadband chirped mirrors (UBCMs). The UBCM coatings were specially designed and manufactured by Hamamatsu Photonics for compressing pulses in visible–near-IR NOPAs. The reflectance band of these mirrors fully supports the signal wave spectrum. The group delay of the UBCMs (dash-dotted curve in Fig. 3) was measured using a white-light interferometer.[28] In addition to contributing approximately a third of the negative dispersion required for pulse compression, these mirrors supply a higher-order phase correction in the spectral wings. The solid curve in Figure 3 indicates the calculated group delay, excluding that of the flexible adaptive mirror. The estimated deviation from the target group delay (shown by the solid circles in Fig. 3), lies

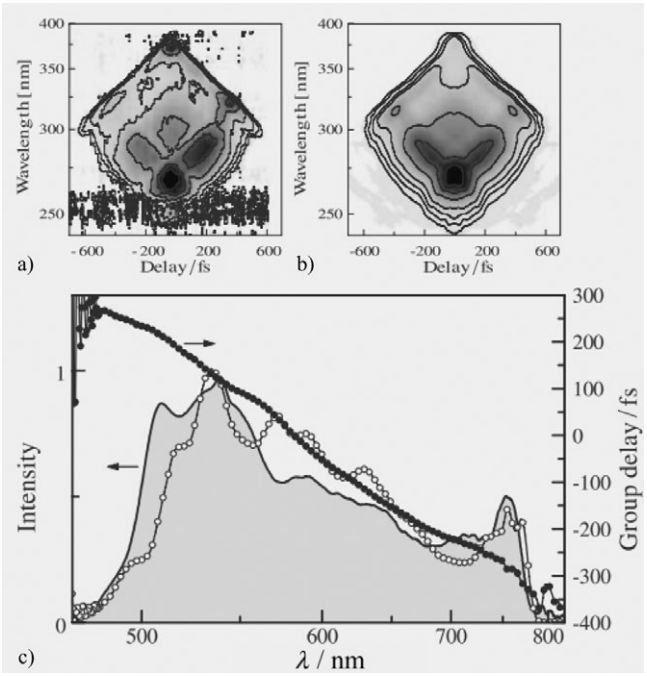

Fig. 4. FROG characterization of chirped amplified pulses. a) Measured FROG trace. b) Retrieved FROG trace. The FROG traces here and elsewhere in the paper are depicted as density plots with contour lines overlaid for FROG peak intensities of 0.02, 0.05, 0.1, 0.2, 0.4, 0.6, and 0.8. c) Retrieved group delay (filled circles) and spectrum (open circles).

within the correction range of the flexible mirror and can be eliminated by varying the shape of the reflective surface.

The micromachined device employed in our study is identical to those used in Refs. [29] and [30]. The membrane is controlled by 39 actuators that are aligned in three rows; it provides a clear aperture of ~30 × 7 mm. Such a modulator can almost completely eliminate smooth variations of the spectral phase that can be described by a cubic spline that passes through 13 nodes, which in this case is distributed over a spectral range of 300 nm. To reduce the number of control parameters from 39 to 13, we fix the actuator voltages that control their vertical movement (i.e., perpendicular to the dispersed beam). This simplification is justified because the surface of the flexible mirror is located in the focal plane of the spherical mirror, which results in a negligibly low sensitivity of the output beam to the actuation in the vertical plane. The channels of the flexible mirror are connected to 8-bit high-voltage drivers, which are controlled by a personal computer (Fig. 1); this allows the voltage of each actuator to be varied in the range 0–280 V. The stiffness of the 0.5-μm-thick silicon-nitride membrane depends on the material and the number of layers of the deposited optical coating. We used an Au coating above a Cr bonding layer, which enables a maximum deflection of over 6 μm in the center of the mirror.

The components of the pulse compressor are positioned on an optical bench in accordance with the ray-tracing calculation results. The distance between the diffraction grating and the spherical mirror was adjusted to within ±1 mm to optimize the SHG signal from a thin frequency-doubling crystal. The final step of pulse compression, namely adaptive phase correction using the flexible mirror, is described as follows.

Adaptive Pulse Shaping

Using a robust adaptive algorithm based on simple spectral measurements, the pulse quality was rapidly (i.e., within several minutes) improved. The inability to remove the remaining discrepancy of the spectral phase arises only from the limited SHG bandwidth. Adaptive phase correction is essential to achieve high-quality compression of extremely broadband laser pulses owing to the complexity of the phase distortion and the limit of conventional pulse compressors in bandwidth and tunability.

Development of a Broadband Detector

To detect weak pump–probe signals at multiple probe wavelengths, we used the multichannel lock-in amplifier shown in Figure 5 for time-resolved spectroscopy. The multi-channel lock-in amplifier was developed in our group. Meanwhile,

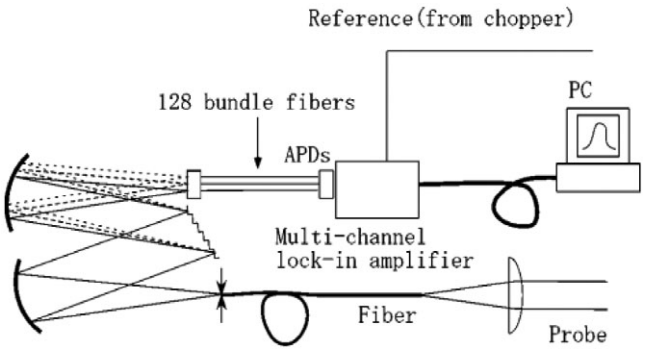

Fig. 5. Schematic of the multichannel lock-in amplifier with a pump–probe measurement system. APDs: avalanche photodiodes; PC: personal computer for data acquisition.

APDs were commercial products optimized for UV to visible light detection (S5343, Hamamatsu Inc.).

The multichannel lock-in amplifier was specially designed to simultaneously detect low-intensity signals at multiple probe wavelengths over the whole probe spectrum. Although multichannel detection of pump–probe signals has already been realized using photodiode arrays or charge-coupled devices, these detectors are less sensitive to low-level signals submerged in a high background, resulting in a lower signal-to-noise ratio than lock-in detection. Multichannel lock-in detection is the natural solution for extracting all the probe information and for avoiding various experimental instabilities, such as sample degradation and laser instability. In this experiment, signals were spectrally resolved by a polychromator (Jasco, M25-TP) at 128 wavelengths in the range 540 to 740 nm and they were detected using avalanche photodiodes and a lock-in amplifier with a reference from an optical chopper that modulated the pump pulse at 210 Hz.

Principles of Real-time Vibration Spectroscopy: Modulation of Electronic Transition Probability by Wave-Packet Motion

This section describes the principles of real-time vibrational spectroscopy. Real-time traces represent the time-dependent intensity being modulated by wave-packet motion generated by the intense pump pulse, whose duration is shorter than the molecular vibrational period. Femtosecond stimulated Raman spectroscopy, which offers high temporal and spectral resolutions, was used to observe time-dependent conformational change.[31] However, femtosecond stimulated Raman spectroscopy measures only the vibration intensity; it cannot provide information on the vibrational phase, which can be obtained by time-resolved difference absorption. Using the ultrashort pulses, ultrafast spectroscopy observes the vibrational phase, which

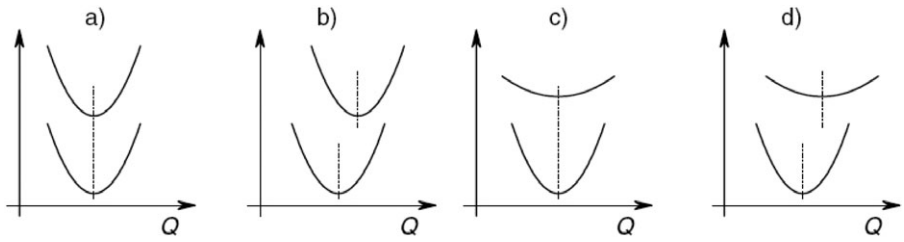

Fig. 6. Four typical cases for the minima and curvatures of the potential curves: a) no change in the potential minimum position or curvature upon photoexcitation; b) a change in potential minimum position with no change in curvature; c) a change in curvature with no change in the potential minimum position; and d) with a change in both the potential minimum position and the curvature. The dash-dotted lines indicate the minimums of the potential surfaces.

helps phenomena associated with the electronic ground state to be distinguished from those associated with the excited state.

In most molecular systems, the wave function of a molecular electronic state can be factorized into the electronic component and the nuclear component using the Born–Oppenheimer approximation (Equation (3)), except when the electronic structure is degenerate:

$$\Psi(q, Q) = \Phi(Q, q)\chi(Q) \tag{3}$$

Here, q and Q represent the electron and nuclear coordinates, respectively. The transition dipole between two electronic states, which can be well described by the Born–Oppenheimer approximation, is given by Equation (4) under the Condon approximation:

$$\begin{aligned} &<\Psi_1(q, Q)|eq|\Psi_2(q, Q)>_{Q,q} = <\chi_1(Q)<\Phi_1(Q, q)|eq| \\ &\quad \Phi_2(Q, q)>\chi_2(Q)>\cong<\Phi_1(Q, q)|eq| \\ &\quad \Phi_2(Q, q)><\chi_1(Q)\,|\,\chi_2(Q)> \end{aligned} \tag{4}$$

The origins of the intensity modulation can be classified into two cases: when the Condon approximation is satisfied and when it is not satisfied. The former case arises from the time-dependent Franck–Condon (FC) overlap as a result of wave-packet formation, the wave function of which is a linear combination of the wave functions of the relevant vibrational levels. The latter case occurs when the electronic wave function is mixed with a third electronic state, which causes the electronic transition probabilities to be exchanged. Following the wave-packet motion, the molecular structure is deformed and the corresponding electronic energies of these states are modified, which modifies the absorption intensity.

When the Condon Approximation Holds

This subsection discusses an electronic transition in a two-level system when the Condon approximation is satisfied. In this case, the integrated intensity of the absorbance change covering the relevant electronic state remains constant during wave-packet motion. The two-level system has two harmonic potential curves for the ground and lowest excited states. Figure 6 shows the potential curves of two electronic states for four typical cases in the present case.

Here, we discuss the wave packet generated only in the ground state; a similar discussion applies when the wave packet is generated in the excited state. There are four typical cases for the minima and curvatures of the potential curves: a) neither the potential minimum position nor the curvature change upon photoexcitation; b) the potential minimum position changes, but the curvature remains the same; c) the curvature changes but the potential minimum position remains the same; and d) both the potential minimum position and the curvature change.

There are four different cases relevant to the above characteristics of the potential curves: a′) generation of a vibrational eigenstate with no wave-packet motion because of the selection rule for allowed transitions; b′) generation of a wave packet in the ground state, which starts to move along the potential curve; c′) generation of a wave packet in the ground state, whose size starts to breathe after photoexcitation; d′) generation of a wave packet in the ground state, which starts to move along the potential curve and breathe at the same time.

Intensity modulation can be introduced by time-dependent overlap of the molecular wave functions between the initial and final electronic states associated with the transition. In such a case, the modulation mechanism for the transition probability is the time-dependent FC overlap factor.

When the molecular vibration is Fourier analyzed to separate many modes into many normal modes, it can be described in terms of a one-dimensional harmonic potential curve. The FC factor is then associated with the motion of a wave packet moving between two equal-energy points on the potential curve along one of the normal coordinates on which the wave packet is located.[32] The time-dependent FC factor, $F(t)$, which is related to the electronic states of the initial and final states

(i and f, respectively) coupled with the transition, is given by Equation (5):

$$F(t) = \sum_l \sum_m c_l^* c_m \left\langle \tilde{\chi}_l^i\left(\hat{Q}\right) \tilde{\chi}_m^f\left(\hat{Q}\right)\right\rangle = \sum_l \sum_m c_l^* c_m \left\langle \chi_l^i\left(\hat{Q}\right) | \chi_m^f\left(\hat{Q}\right)\right\rangle e^{i(l-m)\omega_v t}. \quad (5)$$

Here, $\left|\tilde{\chi}_a\left(\hat{Q}\right)\right\rangle = \left|\chi_a\left(\hat{Q}\right)\right\rangle e^{ia\omega_v t}$ is the nuclear wave function with a vibrational quantum number of $a = (l, m)$, and ω_v is the frequency of the molecular vibration relevant to the vibronic coupling. The linear combination of the time-dependent (oscillating) terms with sets of quantum numbers (l, m) having weight factors related to the FC factor gives the wave-packet motion. The equation describing the spectral change owing to the motion of a wave packet induced by impulsive excitation depends on the FC factor, which is the coefficient of the sinusoidal function in Equation (5). The coefficients $c_l^* c_m$ are determined by the pump laser spectrum and the cross section of the ground state absorption. If i and f are in the ground and excited states respectively, there are two possibilities for the wave packet to be generated by the pump: either in the i state by coherent vibronic excitation or in the f state by the stimulated Raman process. Wave-packet motion then occurs along the potential curve of the corresponding state.

We discuss the case when the potential minimum is displaced along the potential surface of the i state with respect to that of the f state (Fig. 6b). This displaced potential surface case is referred to as the D case in the discussion below about the transition probability modulation mechanism. If the shift owing to wave-packet motion is small, then the spectral change will be small and it can be obtained from the first derivative of the absorption spectrum. Probe wavelength dependence of vibrational amplitude shows a π phase jump at the peak wavelength of the absorption band.[33,34]

When there is no displacement between the ground and excited states (Fig. 6c; referred to as the ND case below) the wave-packet motion does not involve oscillations between two turning points of equal energy on the potential curve of either the excited or ground state. In such a case, the principal wave-packet motion arises from the second-order difference between the initial and final states. The second-order difference is then given by the breathing of the wave packet, in which the width of the wave packet oscillates in time at the vibrational frequency. This mechanism has higher vibronic coupling, with respect to the spectral change, than the FC case as it involves higher order wave-packet motion upon photoexcitation. The initial and final states are expected to have similar potential curves, except when very large geometrical relaxation occurs after excitation. The difference between the potential energies can then be expanded as a Taylor series in terms of the normal coordinate (Q), the nth term of which is proportional to the nth derivative $\left(\frac{\partial^n A(\omega)}{\partial \omega^n}\right)$ of the absorption spectrum ($A(\omega)$).[34] The components of the power series are classified in terms of the vibronic coupling strength. In most cases, the first-order term has the highest coupling strength.

As mentioned above, in the case of breathing, the spectral change is approximately determined by the second derivative of the relevant transition spectrum. When the wave-packet motion is in the ground state, the relevant spectrum is the absorption spectrum for the ground to excited state transition. If the wave-packet motion is in the excited state, then the vibrational amplitude depends on the second derivative of the stimulated emission spectrum and/or the bleaching spectrum.

The above discussion can be expressed by Equation (6), which shows the modulation of the absorbance change ($\Delta A(\omega)$) as a function of the probe frequency ω:

$$\delta\Delta A(t;\Omega,\omega) \cong \Delta A(t;\Omega,\omega) - \Delta A_0(\omega) = \left(\delta\omega \frac{\mathrm{d}\Delta A_0(\omega)}{\mathrm{d}\omega} + \delta\Delta\omega \frac{\mathrm{d}^2\Delta A_0(\omega)}{\mathrm{d}\omega^2}\right)\cos(\Omega t + \phi) \quad (6)$$

Here, Ω is the frequency of the relevant molecular vibrational mode and $\Delta A_0(\omega)$ is the difference absorption spectrum without molecular vibrations. This spectrum can be obtained by smoothing the real-time vibrational trace over several vibrational periods at each probe wavelength. It may be a composite of the gain and bleaching (owing to ground-state depletion) spectra. $\delta\Delta A(\Omega; \omega)$ is the amplitude of the Fourier transformation (FT)) of the absorbance change as a function of the molecular vibrational frequency Ω. $\delta\Delta\omega$ is the change in the bandwidth ($\Delta\omega$) of the absorption, gain or bleaching spectrum.

Up to this point, we have considered the case when the Condon approximation is satisfied. This is referred to as the C mechanism, and it can be sub-classified into D and ND cases. For the D case, the probe frequency dependence of $\delta\Delta A(\Omega; \omega)$ is mainly given by the first derivative of $\Delta A_0(\omega)$, whereas in the ND case, the main contribution is given by the second derivative of $\Delta A_0(\omega)$. The configuration shown in Figure 6d is a mixture of D and ND cases, thus it is expected to have a mixed probe wavelength dependence on the first and second derivatives.

When the Condon Approximation Does Not Hold

In this subsection, deviation from the Condon approximation is introduced by considering another electronic state (a third state) that is radiatively coupled to the other two states between which the transition intensity is being monitored. Here, we discuss a three-level system that includes the third state. The three-level system is composed of three electronic states, S_0, S_1, and S_2 (listed in order of increasing energy). The vibronic coupling is assumed to be predominantly between the S_1 and S_2 states. The following three wave functions are considered:

$$\left|S_0\left(\hat{q},\hat{Q}\right)\right\rangle = \left|\psi_0\left(\hat{q},\hat{Q}\right)\right\rangle\left|\chi_n^0\left(\hat{Q}\right)\right\rangle, \tag{7}$$

$$\left|S_1\left(\hat{q},\hat{Q}\right)\right\rangle = \frac{1}{\sqrt{1+\left(H_{vib}/\Delta E_{21}\right)}}\left(\left|\psi_1\left(\hat{q},\hat{Q}\right)\right\rangle - \frac{H_{vib}}{\Delta E_{21}}\hat{Q}\left|\psi_2\left(\hat{q},\hat{Q}\right)\right\rangle\right)\left|\chi_m^1\left(\hat{Q}\right)\right\rangle, \tag{8}$$

$$\left|S_2\left(\hat{q},\hat{Q}\right)\right\rangle = \frac{1}{\sqrt{1+\left(H_{vib}/\Delta E_{21}\right)}}\left(\left|\psi_2\left(\hat{q},\hat{Q}\right)\right\rangle + \frac{H_{vib}}{\Delta E_{21}}\hat{Q}\left|\psi_1\left(\hat{q},\hat{Q}\right)\right\rangle\right)\left|\chi_m^2\left(\hat{Q}\right)\right\rangle. \tag{9}$$

In the above equations, $\left|\psi_X\left(\hat{q},\hat{Q}\right)\right\rangle$ and $\left|\chi_k^X\left(\hat{Q}\right)\right\rangle$ respectively represent the electron and nuclei wave functions for state X (= 0, 1, and 2 for S_0, S_1, and S_2, respectively) as a function of the electron and nuclear coordinates, $\hat{q}$ and $\hat{Q}$, respectively. In the nuclear wave function $\left|\chi_k^X\left(\hat{Q}\right)\right\rangle$, the vibrational quantum number is denoted by the suffix k (= n and m). ΔE_{21} is the energy difference between states S_2 and S_1 and H_{vib} is the interaction Hamiltonian. The states S_1 and S_2 are not necessarily the first and second excited states but can be any two electronic excited states in general (i.e., the electronic state S_2 can be a higher excited state than the S_1 state). In this way, the spectral change integrated over the relevant spectral range does not have a constant oscillator strength, but rather it varies with the vibrational motion of the mode, whose interaction H_{vib} contributes to the mixing of the two electronic states. The mixing is controlled by the symmetries of the vibrational mode and the electronic states.

Using Equations (7)–(9), the transition dipole moment between $\left|S_0\left(\hat{q},\hat{Q}\right)\right\rangle$ and $\left|S_1\left(\hat{q},\hat{Q}\right)\right\rangle$ can be written as:

$$\begin{aligned}\langle S_0|\mu|S_1\rangle &= \langle\varphi_0|\langle\chi|\mu(|\varphi_1\rangle - \beta Q|\varphi_2\rangle)|\chi_m^1\rangle \\ &= \langle\varphi_0|\mu|\varphi_1\rangle\langle\chi_n^0|\chi_m^1\rangle - \beta\langle\varphi_0|\mu|\varphi_2\rangle\langle\chi_m^0|Q|\chi_m^1\rangle,\end{aligned}$$

$$\beta \equiv \frac{H_{vib}}{\Delta E_{21}}.$$

The transition probability is given by Equation (10):

$$\begin{aligned}|\langle S_0|\mu|S_1\rangle|^2 = {} & |\langle\varphi_0|\mu|\varphi_1\rangle|^2\,|\langle\chi_m^0|\chi_m^1\rangle|^2 - \beta^*\langle\varphi_0|\mu|\varphi_1\rangle \\ & \langle\varphi_0|\mu|\varphi_2\rangle^*\langle\chi_m^0|\chi_m^1\rangle\langle\chi_m^0|Q|\chi_m^1\rangle^* \\ & - \beta\langle\varphi_0|\mu|\varphi_1\rangle^*\langle\varphi_0|\mu|\varphi_2\rangle \\ & \langle\chi_m^0|\chi_m^1\rangle^*\langle\chi_m^0|Q|\chi_m^1\rangle + \text{h.o.}\end{aligned} \tag{10}$$

The discussion becomes complicated when both $S_0 \rightarrow S_1$ and $S_1 \rightarrow S_2$ are allowed transitions. Therefore, we utilize the modified phenomenological equation (Equation (6)) as Equation (11):

$$\delta A(t;\Omega,\omega) \cong \left(\frac{\delta(\mu^2)}{\mu^2}\Delta A_0(\omega) + \delta\omega\frac{\mathrm{d}\Delta A_0(\omega)}{\mathrm{d}\omega} + \delta\Delta\omega\frac{\mathrm{d}^2\Delta A_0(\omega)}{\mathrm{d}\omega^2}\right)\cos(\Omega t,\phi). \tag{11}$$

The first term represents the modulation of the transition dipole moment μ of the relevant electronic transition.

The non-conserved oscillator strength will make the Condon approximation invalid, which implies that the integrated intensity over the electronic transition is not constant during the vibrational period (this is referred to as the non-Condon (NC) mechanism below). This mechanism can also be sub-classified into D and ND cases.

The dependence of $\delta\Delta A(\Omega;\omega)$ on the probe photon frequency for the NC mechanism is given as follows. For the D case, $\delta\Delta A(\Omega;\omega)$ depends on the zeroth and first derivatives of $A_0(\omega)$, whereas it depends on the zeroth and second derivatives of $A_0(\omega)$ for the ND case. For both the D and ND cases for the NC mechanism, the zeroth-order dependence of the probe wavelength was added to fulfill the non-conserved integrated transition probability in the NC mechanism. The zeroth-order derivative can also be understood as the time-dependent contribution of the third electronic state, which varies periodically with the vibrational frequency. These phenomena have been described as alternating intensity borrowing and returning.[35,36,37]

Classification of the Vibrational Modes

The real-time vibration spectroscopy, theoretically discussed in sections describing when the Condon approximation holds and does not hold, was demonstrated for a sample molecule of a quinoidal thiophene derivative QT2.[37] The representative vibrational modes can be classified based on the above discussion. There are several modes that can be classified in the C mechanism. Their integrated intensities remain constant during the molecular vibration. They have frequencies of 301, 1172, 1343, 1420, and 1453 cm^{-1}. The remaining modes, with frequencies of 785, 1376, and 1539 cm^{-1}, are classified in the NC mechanism because the Condon approximation does not hold owing to the change in the transition probability integrated over the transition band. A detailed data analysis and discussion about this classification is given in Ref. [38]. Table 1 summarizes the results of the classification.

Examples of Real-Time Spectroscopy Applications

Primary Conformation Change in Bacteriorhodopsin upon Photoexcitation

Photoisomerization of rhodopsin is the key reaction in the vision process. However, ultrafast time-resolved observation

Table 1: Mode classification in terms of vibronic coupling mechanisms.

Frequency (cm^{-1})		VC[b]	PS[c]	Sym[d]	Modes[e]
FT (CAL)[a]	FT–CAL				
301 (303)	–2	C-1	D	u	α
785 (773)	12	NC-0	ND	g	α
1172 (1161)	11	C-2	ND	N	β (benzene)
1343 (1343)	0	C-1	D	u	δ (CH_2); γ (benzene CH)
1376 (1407)	31	NC-0,1	D	g	ε(CH_2); ρ_s C=C
1420 (1425)	–5	C-1,2	D+ND	u	ε(CH_2); ρ_{as} C=C
1453 (1475)	–22	C-1w,2	ND	N	γ(benzene CH); ν C=C
1539 (1549)	–10	NC-0,2w	ND	g	ν C=C

[a]FT: frequencies obtained from the FT of the real-time trace; CAL: frequencies obtained from the quantum chemical calculation. [b]VC: vibronic coupling; C: Condon mechanism; NC: non-Condon mechanism; 0, 1, 2: derivative order; w: relatively weak contribution. [c]PS: potential surface; D: displaced case; ND: non-displaced case. [d]Sym: symmetric (g: gerade (symmetric); u: ungerade (antisymmetric); N: no well-defined symmetry with an inversion center, but a mixture of g and u). [e]α = in-plane skeletal; β = skeletal; δ = twisting; γ = bending; ε = wagging; ρ = degenerate bending; ν = stretching.

of this process is difficult because rhodopsin does not recover after in vitro photobleaching. The membrane protein bacteriorhodopsin (bR),[39,40] which is extracted from bacteria, is more stable than artificial chemicals, making it a promising functional material for optical memories and switches.[41] The physiological function of bR in live bacteria is proton pumping to produce a chemical potential for ATP synthesis. This pump is optically triggered by *trans–cis* photoisomerization, which is closely related to *cis–trans* photoisomerization of rhodopsin in the vision process.[42] As a result of these interesting physiological and artificial functionalities, the primary process of bR has been extensively studied both theoretically[43,44] and experimentally.[45,46,47,48,49,50,51]

Most studies consider the process to be as follows:

$$\mathrm{bR} \rightarrow \mathrm{H}\text{—}(200\ \mathrm{fs}) \rightarrow \mathrm{I}\text{—}(500\ \mathrm{fs}) \rightarrow \mathrm{J}\text{—}(3\ \mathrm{ps}) \rightarrow \mathrm{K}$$

However, some controversial experimental results have been reported. For example, Ruhman's group showed experimentally that the locked-retinal chromophore contained in bR exhibits a similar photoinduced spectral change to that of ordinary bR.[52,53]

Atkinson's group claimed that the long-accepted isomerization process does not occur in the primary process, even in the J intermediate.[54] The J intermediate is often assigned as a ground-state species in which the retinal chromophore is isomerized to a 13-cis configuration, as first proposed by Ruhman and co-workers. Furthermore, two theoretical models of photoisomerization have been proposed, namely a two-state, two-mode model and a three-state model proposed by Olivucci's[55] and Schulten's groups;[56] it still remains unclear which model is correct. Recent studies of photoisomerization of a retinyl chromophore have shed light on the dynamics after photoexcitation;[57,58] however, the details of the transient states still remain a topic of contention.

The reason why the photoisomerization yield of bR is about 0.67 is explained as follows. An excited-state wave packet oscillates with a period of ~400 fs on the potential surface of the excited state. When it crosses the bottom of the potential surface in the direction to form the J intermediate (or initial ground state), the excited population has an opportunity to cross the conical intersection into the J state (or the initial ground state). This is why some excited bR reverts back to the initial ground state. Clarification of these ultrafast dynamics requires direct observation of the TS in photoisomerization.

As discussed in a recent study,[54] time-resolved absorbance change measurements measure the contribution of wave packets on the potential surfaces of the electronic ground and excited states. There are three ways to distinguish a ground state signal from an excited state signal. One method is time-resolved spectroscopy using chirped pump pulses, which was performed by Kahan and co-workers.[52] Another method is to observe the vibrational phase of a molecular vibration. The motion of a ground-state wave packet commences from a stable local minimum point on the ground-state potential-energy surface, whereas an excited-state wave packet starts its motion from the Franck–Condon state toward a local minimum point on the excited-state potential-energy surface. Therefore, vibrations of wave packets on the potential surfaces of the ground and excited states are expected to be sine-like and cosine-like, respectively. The third method is to observe the dependences of the signal on the probe wavelength and the delay. Using intermediate lifetimes determined in previous studies, decay of the transient absorption signal can determine the dominant intermediates in different probe wavelength regions. The sign of the signal also helps assign the origin of the signal: a negative absorbance change indicates that photobleaching is caused by depletion of the electronic ground state or stimulated emission from the excited state, whereas a positive absorbance change

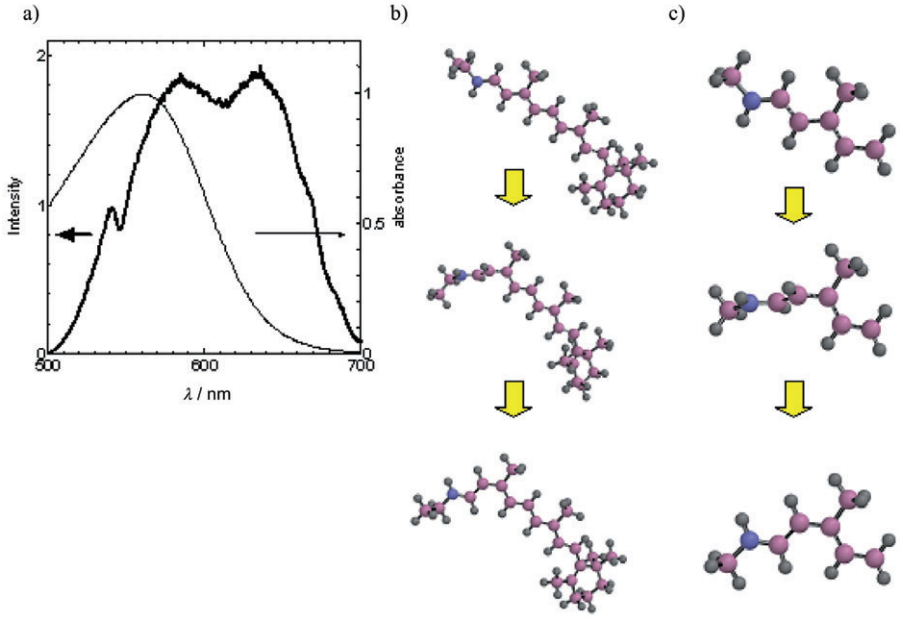

Fig. 7. Laser spectrum, absorption spectrum of bR, and molecular structure of the retinal chromophore in bR. a) Laser spectrum (thick line) and absorption spectrum of bR (thin line). b) Schematic conformational change in the *trans–cis* photoisomerization of the retinal chromophore in bR (CIS/6-31G*//CIS/6-31G*). c) Enlarged views of molecular structures around C_{13}=C_{14} and C_{15}=N shown in (b). The purple and blue balls in (b) and (c) represent carbon and nitrogen atoms, respectively. The first, second, and third models in (c) are related to the structure of the H, I, and J states, respectively.

indicates induced absorption from the first excited state to a higher excited state.

Femtosecond stimulated Raman spectroscopy that has high temporal and spectral resolutions was used to observe time-dependent conformational changes. The femtosecond stimulated Raman spectroscopy measures only the vibration intensity but cannot provide information on the vibrational phase. Using the ultrashort pulses, vibrational real-time-resolved absorbance change measurement can provide the initial vibrational phase, which can be used for the assignment of the vibrational mode either to the electronic ground state or to the excited state.

In our study, the experimental technique used for ultrafast spectroscopy was improved over that used in our previous study.[59] The second and third methods mentioned above were used with ultrashort laser pulses and their spectra are shown in Figure 7a. The experimental results contain a lot of information about the sample dynamics, which can be obtained from continuous spectra and time-dependent (including vibrational phase) transmittance changes at all wavelengths. Simultaneous measurement at all the probe wavelengths enables measurements to be performed much faster than previous time-consuming measurements at five different wavelengths.[59] The simultaneous measurement reduced systematic errors arising from short- and long-term fluctuations in the laser intensity and also sample degradation, which is inevitable in experiments requiring long measurements.

The obtained data reveal the detailed photoexcited dynamics of the retinal chromophore in bR during photoisomerization. This technique has the potential to overcome the problems associated with the other two methods mentioned above. Fig. 7b shows the structural change of a retinal chromophore during photoisomerization. The structural changes in the retinal chromophore were calculated to obtain schematic views that depict the structural changes in a retinyl chromophore in bR; however, the calculated structure may differ slightly from that of a retinyl chromophore in bR, which is known to have a twisted conformation even in the K state.[59,60] The time constants for transitions from the ground state to the intermediate states I, J, and K determined from experimental results are consistent with the results obtained in studies by other groups.[53,61] The probe wavelength dependence of the photoexcited dynamics was analyzed and it was found that the probe wavelength spectrum can be classified into four spectral regions based on the dynamics. This is because the electronic states have different effects on each spectral region. For the same reason, the dynamics of the molecular vibrational modes was also considered to be dependent on the probe wavelength. Diller and co-workers found that the C=N stretching mode appears earlier than 500 fs after photoexcitation.[46] The present

analysis of molecular vibrational modes reveals the existence of the C=N stretching mode, which decays within 30 fs after photoexcitation. This implies that the primary event immediately after photoexcitation is not the excitation of torsion around the C_{13}=C_{14} bond, as has long been believed,[62] nor is it the C=C stretching mode, as was recently proposed.[43]

The spectrograms (Figures 8a–d) reveal the existence of a C=N stretching mode with a frequency of ~1640 cm^{-1}, whose vibration period is 20 fs. The C=N signal disappears after 30 fs. Because of the short lifetime of this mode, which corresponds to 1.5 oscillation periods, the Raman spectrum is expected to have a broad bandwidth of about 1100 cm^{-1}, which reduces the peak intensity by a factor of about 100 from that estimated from the Raman spectral width of the C=N mode in the ground state.[63] From the line width of the ground-state Raman signal of bR,[65] the decay time of the C=N stretching mode in the ground state is known to be slightly longer than 3 ps. The observed C=N signal decays much faster (<30 fs) than the appearance time (>200 fs) of the I state. Therefore, the observed Fourier signal of the C=N stretching frequency is thought not to arise from the G or I state. Rather, it is thought to be attributed to the H state, which is excited in the very initial stages of photoisomerization. The excited molecular vibration of the C=N stretching mode decays rapidly (<30 fs) in the H state, indicating that the C=N vibration oscillates less than two times. The H state then decays with a time constant of 235 ± 22 fs. This finding can explain the very interesting but controversial observation by Ruhman's group.[53] Even the locked retinal analogue can be deformed near the protonated C=N bond, resulting in spectral changes similar to those induced by isomerization. Therefore, the spectral changes commonly observed both in native retinal and the artificial locked analogue are introduced by electronic changes near the protonated C=N bond, rather than the C_{13}=C_{14} bond. After this conformational change near the C=N bond, the vibration of which is heavily damped, C=C stretching and torsion around the C_{13}=C_{14} bond start.

Mathies' group[39] found that the I state appears within about 200 fs. The positive ΔA about 200 fs after photoexcitation in the 610–630 nm and 635–664 nm spectral ranges indicate the contribution of the induced absorption owing to the I state. In the probe spectral ranges, a new signal appears around 1800 cm^{-1} about 200 fs after excitation (Figs. 8e and f), indicating that the signal is mainly arising from the I state. This new mode is possibly related to highly distorted C=N stretching. The increase in the C=N stretching frequency to about 1800 cm^{-1} indicates that π-electron flow to the protonated Schiff base after the very rapid distortion partially neutralizes the positive charge of the N atom, increasing the bond order. This implies that the charge redistribution occurs from interaction with binding pocket residues and that the distortion relaxes on formation of the J intermediate.

Based on the results of our study, it is concluded that the first process in the photophysical dynamics in bR is the deformation of the retinal configuration which decays within 30 fs near the C=N bond in the protonated Schiff base. It is followed by C=C stretching and then tortional motion of several periods around the C_{13}=C_{14} bond. This mode is as short as 30 fs, which corresponds to only 1.5 times the oscillation period (20 fs). This means that electronic redistribution, which occurs immediately after excitation (<2 fs), triggers rapid oscillation of C=N stretching. After a few oscillations, the energy is transferred to C=C stretching.

Direct Observation of Molecular Structural Changes During Claisen Rearrangement

The Claisen rearrangement is one of the most well-known sigmatropic rearrangements in organic chemistry. Along with the Cope rearrangement, it is known for its high stereoselectivity making it an extremely useful technique in organic synthesis. [3,3] sigmatropic rearrangements of allyl aryl (or vinyl) ethers reported by L. Claisen[64] spurred the development of various other reactions.[65,66,67] In 1938, allyl vinyl ether (AVE) was found to generate allyl acetaldehyde when it was heated at 255 °C through [3,3] sigmatropic rearrangement (Figure 9).[68]

The Claisen rearrangement is thought to proceed via a six-membered TS by a supra–supra facial reaction following Woodward–Hoffmann rules[69] and frontier orbital theory.[70] Experimental stereochemical[71,72,73,74] results and theoretical calculations[75,76,77] suggest a six-membered chair-form TS. However, a more detailed mechanism for the Claisen rearrangement still remains controversial (Fig. 9). In one possible mechanism, the reaction progresses in a synchronous concerted pathway via an aromatic-like TS.[78] In another possible mechanism, the reaction progresses by an asynchronous concerted pathway in which either C^1–C^6 bond formation or C^4–O bond breaking occurs before the other process. An asynchronous reaction in which the C^1–C^6 bond forms first may proceed through a 1,4-diyl-like TS,[79,80] whereas an asynchronous reaction in which the C^4–O bond breaks first may proceed through a bis-allyl-like TS.[81,82,83,84,85,86,87] As the simplest example of the Claisen rearrangement, AVE was studied by performing quantum chemical calculations and by using the kinetic isotope effect (KIE). By observing the secondary isotope effect using deuterium, Gajewski and co-workers concluded that C^4–O bond breaking occurs first to generate a bis-allyl-like TS.[81,84] Singleton and co-workers claimed that theoretical calculations and the KIE suggest the possibility of variations in the 1,4-diyl and bis-allyl characters;[87] however, the aromaticity of the TS was not ruled out, because it was necessary to describe the TS geometry. On the other hand, many theoretical calculations based on various methods have produced conflicting results.[78,80,81,82,85,87,88]

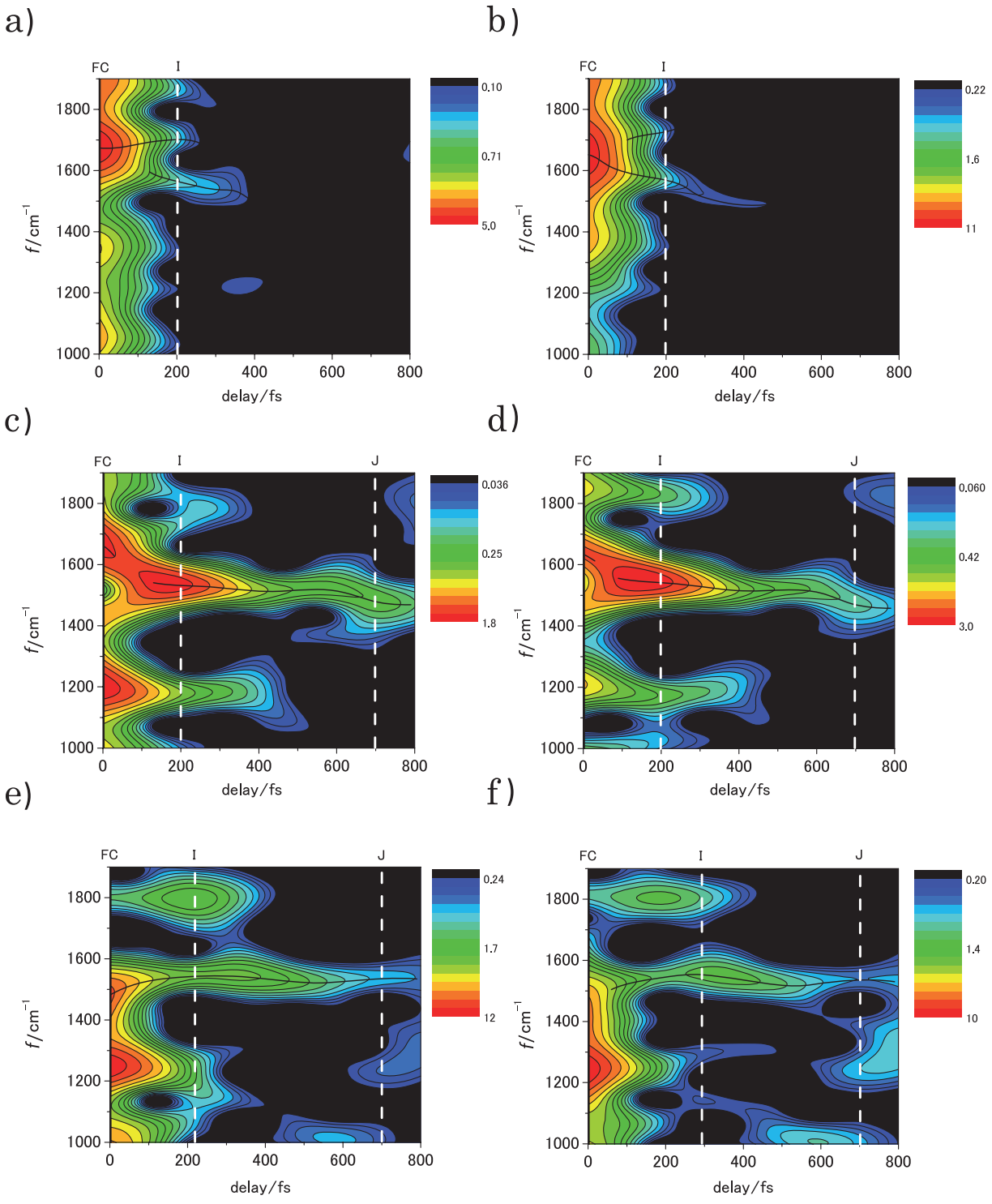

Fig. 8. Spectrograms calculated from the real-time traces measured at (a) 512, (b) 517, (c) 572, (d) 577, (e) 617, and (f) 622 nm. The white broken lines in the figures indicate the approximate appearance times of the H, I, and J states.

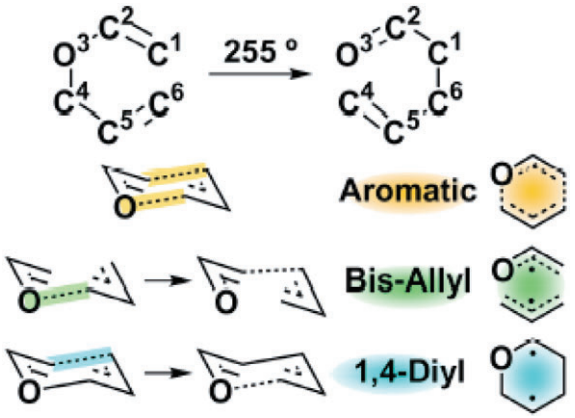

Fig. 9. Three proposed transition states of the Claisen rearrangement of AVE. The aromatic-like TS appears in the synchronous concerted process. The bis-allyl-like and 1,4-diyl-like TSs appear in the asynchronous concerted process in which either C^4–O bond breaking or C^1–C^6 bond formation occurs before the other process.

KIE and theoretical calculations cannot provide information on dynamics; they can only predict the molecular structures of the rate-determining step and of the most stable TS, respectively. Therefore, it is not easy to determine chemical reaction pathways, including TSs, based only on KIE or theoretical calculations, and detailed structures of TSs remain elusive. For this reason we have used a 5-fs pulse laser developed by our group to observe molecular structural changes during the rearrangement process, including the TS, through instantaneous molecular vibration frequencies, which enabled us to elucidate the reaction mechanism.[88]

AVE has an absorption peak at a wavelength shorter than 220 nm, which cannot be reached either by one-photon or two-photon absorption of visible 5-fs laser pulses, whose spectrum extends from 525 to 725 nm. Therefore, a 5-fs pulse triggers coherent molecular vibrations through the stimulated Raman process in the electronic ground state and the thermal reaction does not cause electronic excitation or photochemical reaction.[89]

Using the observed absorbance difference, spectrogram analysis[90] was performed by a sliding-window Fourier transform with a Blackman window function with a full width at half maximum (FWHM) of 400 fs (Figure 10). Molecular structure deformation during the reaction process along the reaction coordinate alters the vibrational frequency of the wave packet vibrating along the coordinate perpendicular to the reaction coordinate. There are $3N$–7 coordinates perpendicular to the reaction coordinate in a molecule composed of N atoms with $3N$–6 normal modes. Therefore, when the molecule is between the reactant, the intermediate, and the product, the vibration frequencies are thought to keep shifting in the spectrogram. If the molecule stays in the reactant, the intermediate, or the

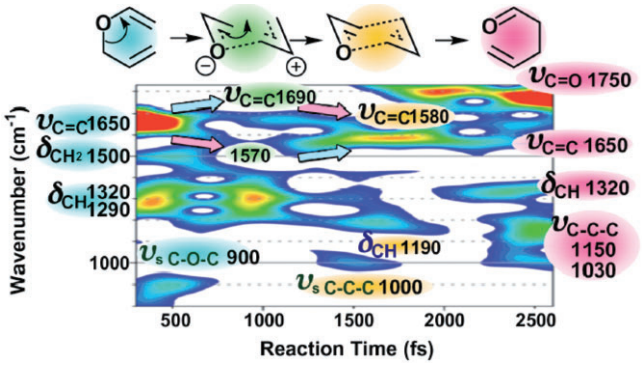

Fig. 10. Spectrogram using a Blackman window function with a FWHM of 400 fs.

product, the vibrational frequencies are thought to remain constant during the lifetime of the relevant state. However, it is difficult to discuss in detail the amplitude of $\delta(\Delta A)$ arising from molecular vibrations since it depends not only on modulation of the electronic transition probability but also on the vibronic coupling strength that induces the modulation.

In the spectrogram, the molecular vibrational modes immediately after photoexcitation only arise from the reactant AVE. However, new bands appear at a delay of 2 ps. These new bands are assigned to the C=O stretching mode ($\nu_{C=O}$), the C–C–C symmetric stretching mode ($\nu_{s\,C-C-C}$), and the C–C–C asymmetric stretching mode ($\nu_{as\,C-C-C}$) at 1750, 1030, and 1150 cm^{-1}, respectively. The frequencies of these new modes correlate well with the frequencies of the Raman spectrum of allyl acetaldehyde, which was synthesized independently by oxidizing 4-penten-1-ol. The appearance of these new modes confirms that allyl acetaldehyde was generated. For comparison with the above data, we performed pump–probe measurements of the independently synthesized product (allyl acetaldehyde). The observed frequencies in the fast Fourier transform power spectrum of the allyl acetaldehyde agree well with the frequencies observed at 2 ps in the spectrogram of AVE. This result strongly supports our conclusion that allyl acetaldehyde is generated in the vibration excitation of AVE with the 5-fs pump pulse. Furthermore, the NMR spectrum of AVE after the pump–probe experiment also demonstrates generation of allyl acetaldehyde. We performed a pump–probe experiment with a small amount of AVE in a glass cell (10 mm^3). The NMR spectrum of AVE after the measurement revealed the presence of allyl acetaldehyde at a fraction of 1% w/w. The quantum yield of the photoinduced process was estimated to be about 0.1. As mentioned above, time-resolved observations of the molecular vibrations reveal molecular structure changes during the Claisen rearrangement.

The detailed mechanism of the reaction was thus clarified. The disappearance of the $\nu_{s\,C-O-C}$ (890 cm^{-1}) and the δ_{CH2}

(1500 cm^{-1}) bands at about 800 fs reveals that the C^4–O bond is weakened or broken in the first step of the reaction. The frequency shift of $\nu_{C=C}$ also suggests that the C^4–O bond is weakened. $\nu_{C=C}$ of the vinyl and allyl groups, observed at 1650 cm^{-1} immediately after photoexcitation, separates into a blue-shifted mode that moves toward 1690 cm^{-1} and a red-shifted mode that moves toward 1570 cm^{-1} as the probe delay time is increased from 500 to 800 fs. These frequency shifts suggest that the C^4–O bond weakening or breaking caused the electronic density in the vinyl and allyl groups to increase and decrease, respectively.

After C^4–O bond weakening, an electron is transferred from the vinyl group to the allyl group to form a weak C^1–C^6 bond. This reduces the electronic density along the C^1=C^2 bond in the vinyl group resulting in a red shift of $\nu_{C=C}$. In the allyl group, the electronic density along the C^5=C^6 bond is increased to induce the blue shift of $\nu_{C=C}$, and the C^4–C^5 single bond changes to a C^4=C^5 double bond. This makes the three C=C bonds in the vinyl and allyl groups (i.e., C^1=C^2, C^4=C^5, and C^5=C^6) equivalent and they have the same frequency of 1580 cm^{-1} at about 1500 fs delay. The appearance of a band at around 1580 cm^{-1} indicates that aromatic C=C bonds are formed since the aromatic $\nu_{C=C}$ in benzene has a frequency of 1585 cm^{-1}, which implies that the generated intermediate does not have the perfect C6 symmetry of a benzene ring, but an aromatic-like six-membered structure. This conclusion is also supported from the appearance of δ_{C-H} and $\nu_{s\ C-C-C}$ at 1190 and 1000 cm^{-1}, respectively (δ_{C-H} of benzene is observed at 1180 cm^{-1}). Finally, C^4–O bond breaking and C^1–C^6 bond formation proceed simultaneously (i.e., in a synchronous concerted process) to generate the product, allyl acetaldehyde.

Calculations of optimized TS geometric and intrinsic reaction coordinates (IRC) were performed using B3LYP/6-311+G**.[91] The change in the bond length calculated by IRC is fully consistent with the result obtained by the 5-fs pump–probe experiment. The pump–probe experiment suggests a three-step pathway, whereas the IRC calculation suggests an asynchronous concerted process.

As mentioned above, the Claisen rearrangement is one of the most useful techniques in chemical synthesis, but the transition state of the reaction has remained controversial for a long time owing to the difficulties associated with directly observing it. Our study has revealed that the reaction mechanism, including the TS, is more complex than that predicted by theory. The observed structural changes during the reaction process imply that the Claisen rearrangement follows a three-step pathway, which includes both a stepwise process and a concerted process. In the first step, the C^4–O bond is weakened to generate a bis-allyl-like intermediate. Next, the formation of a weak C^1–C^6 bond results in the generation of an aromatic-like intermediate. Finally, C^4–O bond breaking and C^1–C^6 bond formation progress simultaneously (i.e., in a concerted process) to generate the product allyl acetaldehyde. Thus, the first two steps are stepwise, whereas the last step proceeds as a synchronous, concerted process. An aromatic-like intermediate is generated after the generation of the bis-allyl-like intermediate because of the high stability of aromatic-like six-membered structures.

Summary and Future Prospects

Development of ultrashort laser pulses meets many needs in various scientific fields as demonstrated by their wide variety of applications, including for defining frequency standards, for distance measurements, and for studying the ultrafast dynamics of chemicals, biological materials, and solid-state/condensed matter physics. Using sub-5-fs pulses, we found various new phenomena, such as dynamic mode coupling between molecular vibrational modes,[92] dynamics observation of Duschinsky rotation,[93] and a dynamic intensity borrowing effect.[35,36,37] In this review, we have introduced several typical achievements that we obtained by ultrafast time-resolved spectroscopy.

Firstly, we discussed the dynamic vibronic couplings in vibrational real-time spectra of a thiophene derivative (QT2). Pump-probe spectroscopy was performed for the sample with a few cycle pulses of 6.7 fs duration. The real-time vibrational features were analyzed in terms of the dependence of vibrational amplitude and phase on probe photon energy. It demonstrated that the dynamic vibronic couplings can be classified by analyzing the results of ultrafast time-resolved spectroscopy.

Secondly, the ultrafast dynamics in photoisomerization of a biopolymer (bR) were presented. We directly observed the instantaneous vibration spectrum deformed by the rotation in the retinal chromophore. We succeeded in observing vibrational spectra that reflect the molecular structure of transition states, and applied this technique to a protein that has a complex molecular structure. In ultrafast and broadband spectroscopy of bR, we found that the frequency of the C=C stretching mode was modulated along with the torsion motion around C_{13}=C_{14} during photoisomerization of bR. This reveals that the bond length of C_{13}=C_{14} is modulated on the deformation around C_{13}=C_{14} during photoisomerization.[16] Ultrafast spectroscopy was also used for direct observations of microstructure changes, which have been only predicted theoretically, like the initial structural change in photobiological processes such as photoisomerization in rhodopsin, bR,[94] and photodissociation of oxygen from oxyhemoglobin.[95]

Finally, we have shown the result of direct observation of a transition state during Raman-excited oxidation of chloroform.[96] The obtained result demonstrated that the observation of transition states by sub-5-fs time-resolved spectroscopy is applicable for ground-state reactions as well as for excited-state

reactions via Raman excitation in a wide variety of chemical reactions.

As presented above, stable ultrashort visible pulses and simultaneous detection in the broadband spectral region enable us to perform highly reliable time-resolved vibration spectroscopy. This advantage allows us to apply the methodology of ultrafast dynamics study even for materials which have constraint in their measurement, like biomaterials. As a future prospect of this work, we show the current application of this ultrafast broadband spectroscopy system, and then, its further improvement and expansion will be discussed.

Real-time observation of vibration modes in electronic ground and excited states of condensed matter like molecules, polymers, and biopolymers is one of the applications of the ultrafast spectroscopy study. In this field, it is thought that there are still many more interesting phenomena that have not yet been observed. For example, observation of the real-time vibration spectrum clarifies conformation information of the transition state when the chemical reaction proceeds from initial state to product proceeding via intermediates. Thus, real-time observation of molecular vibration in the transition state will elucidate the whole picture of a chemical reaction.

Another application of the ultrafast broadband measurement system is for spectroscopy as a replacement for a common Raman spectroscopy method of Raman excitation profile. Traditionally, to find which electronic states are involving Raman modes via vibronic coupling, excitation wavelength dependency of those Raman modes should be studied by changing the wavelength of the Raman excitation light source. Generally speaking, a Raman excitation laser has high spectral purity, however its wavelength is hard to be tuned. Moreover, laser intensity at the tuned wavelength should be measured to correct the data of excitation wavelength dependency. Therefore, it is highly time-consuming to observe the excitation wavelength dependency of the Raman intensity at a significant number of excitation wavelengths, which results in calling the reliability of the correction in question. This is the reason why the Raman excitation wavelength dependency has been rarely studied even though the method was proposed many years ago. The time-resolved broadband spectroscopy developed in this work does not have those weak points, being a powerful tool to study vibronic coupling characters of vibration modes.

Acknowledgments

The authors would like to thank Profs. A. Baltuska and E. Tokunaga and Drs. Z. Wang, Y. Wang, and I. Iwakura for their collaborations on the subjects described here. This work was supported by the International Cooperative Research Project (ICORP) program of the Japan Science and Technology Agency (JST), National Science Council of the Republic of China, Taiwan (NSC 98-2112-M-009-001-MY3), and a grant from the Ministry of Education, Aiming for Top University (MOE ATU) Program at National Chiao-Tung University (NCTU). A part of this work was performed under the joint research project of the Institute of Laser Engineering, Osaka University under Contract No. B1-27, and a Grant-in-Aid for Scientific Research from the Japan Society for the Promotion of Science (JSPS-GASR-14002003).

REFERENCES

[1] T. S. Rose, M. J. Rosker, A. H. Zewail, *J. Chem. Phys.* **1988**, *88*, 6672.
[2] J. C. Polanyi, A. H. Zewail, *Acc. Chem. Res.* **1995**, *28*, 119.
[3] F. Schotte, J. Soman, J. S. Olson, M. Wulff, P. A. Anfinrud, *J. Struct. Biol.* **2004**, *147*, 235.
[4] B. J. Siwick, J. R. Dwyer, R. E. Jordan, R. J. D. Miller, *Science* **2003**, *302*, 1382.
[5] R. Srinivasan, J. S. Feenstra, S. T. Park, S. Xu, A. H. Zewail, *Science* **2005**, *307*, 558.
[6] T. Kobayashi, T. Saito, H. Ohtani, *Nature* **2001**, *414*, 531.
[7] A. Shirakawa, I. Sakane, M. Takasaka, T. Kobayashi, *Appl. Phys. Lett.* **1999**, *19*, 2268.
[8] A. Baltuska, T. Kobayashi, *Appl. Phys. B* **2002**, *75*, 427.
[9] A. Baltuska, T. Fuji, T. Kobayashi, *Opt. Lett.* **2002**, *27*, 306.
[10] G. Cerullo, M. Nisoli, S. De Silvestri, *Appl. Phys. Lett.* **1997**, *71*, 3616.
[11] T. Wilhelm, J. Piel, E. Riedle, *Opt. Lett.* **1997**, *22*, 1494.
[12] J. Piel, M. Beutter, E. Riedle, *Opt. Lett.* **2000**, *25*, 180.
[13] T. Kobayashi, H. Wang, Z. Wang, T. Otsubo, *Chem. Phys. Lett.* **2006**, *426*, 105.
[14] T. Kobayashi, H. Wang, Z Wang, T. Otsubo, *J. Chem. Phys.* **2006**, *125*, 044103.
[15] Z. Wang, T. Otsubo, T. Kobayashi, *Chem. Phys. Lett.* **2006**, *430*, 45.
[16] T. Kobayashi, A. Yabushita, T. Saito, H. Ohtani, M. Tsuda, *Photochem. Photobiol.* **2007**, *83*, 363.
[17] T. J. Driscoll, G. M. Gale, F. Hache, *Opt. Commun.* **1994**, *110*, 638.
[18] G. M. Gale, M. Cavallari, T. J. Driscoll, F. Hache, *Opt. Lett.* **1995**, *20*, 1562.
[19] G. Cerullo, M. Nisoli, S. Stagira, S. De Silvestri, *Opt. Lett.* **1998**, *23*, 1283.
[20] P. Di Trapani, A. Andreoni, C. Solcia, P. Foggi, R. Danielis, A. Dubietis, A. Piskarskas, *J. Opt. Soc. B* **1995**, *12*, 2237.
[21] G. M. Gale, F. Hache, M. Cavallari, *IEEE J. Sel. Topics Quantum Electron.* **1998**, *4*, 224.
[22] E. Riedle, M. Beutter, S. Lochbrunner, J. Piel, S. Schenkl, S. Spoerlein, W. Zinth, *Appl. Phys. B* **2000**, *71*, 457.
[23] G. Cerullo, M. Nisoli, S. Stagira, S. De Silvestri, G. Tempea, F. Krausz, K. Ferencz, *Opt. Lett.*, **1999**, *24*, 1529.
[24] G. Cerullo, M. Nisoli, S. Stagira, S. De Silvestri, G. Tempea, F. Krausz, K. Ferencz, *Appl. Phys. B* **2000**, *S70*, S253.
[25] A. Shirakawa, T. Kobayashi, *Appl. Phys. Lett.* **1998**, *72*, 147.

[26] A. Shirakawa, I. Sakane, T. Kobayashi, *Opt. Lett.* **1998**, *23*, 1292.
[27] R. Danielius, A. Piskarskas, P. Di Trapani, A. Andreoni, C. Solcia, P. Foggi, *Opt. Lett.* **1996**, *21*, 973.
[28] A. P. Kovacs, K. Osvay, Z. Bor, R. Szipöcs, *Opt. Lett.* **1995**, *20*, 788.
[29] E. Zeek, K. Maginnis, S. Backus, U. Russek, M. Murnane, G. R. Mourou, H. Kapteyn, G. Vdovin, *Opt. Lett.* **1999**, *24*, 493.
[30] E. Zeek, R. Bartels, M. Murnane, H. Kapteyn, S. Backus, *Opt. Lett.* **2000**, *25*, 587.
[31] D. W. McCamant, P. Kukura, R. A. Mathies, *Appl. Spectrosc.* **2003**, *57*, 1317.
[32] J. B. Renucci, W. Richter, M. Cardona, E. Schöstherr, *Phys. Status Solidi b* **1973**, *60*, 299.
[33] A. T. N. Kumar, F. Rosca, A. Widom, P. M. Champion, *J. Chem. Phys.* **2001**, *114*, 701.
[34] N. Ishii, E. Tokunaga, S. Adachi, T. Kimura, H. Matsuda, T. Kobayashi, *Phys. Rev. A* **2004**, *70*, 023811.
[35] H. Kano, T. Saito, T. Kobayashi, *J. Phys. Chem. A* **2002**, *106*, 3445.
[36] H. Kano, T. Saito, T. Kobayashi, *J. Phys. Chem. B* **2001**, *105*, 413.
[37] H. Kano, T. Kobayashi, *J. Chem. Phys.* **2002**, *116*, 184.
[38] T. Kobayashi, Z. Wang, T. Otsubo, *J. Phys. Chem. A* **2007**, *111*, 12985.
[39] W. T. Pollard, C. H. Brito Crus, C. V. Shank, R. A. Mathies, *J. Chem. Phys.* **1988**, *88*, 199.
[40] D. Oesterhelt, W. Stoeckenius, *Methods of Enzymology, Biomembranes Part A* Vol. *31*, **1995**, Academic Press: New York.
[41] Y. Huang, S. T. Wu, Y. Zhao, *Opt. Exp.* **2004**, *12*, 895.
[42] A. P. Shreve, R. A. Mathies, *J. Phys. Chem.* **1995**, *99*, 7285.
[43] R. Gonzáles-Luque, M. Garavelli, F. Bernardi, M. Merchan, M. A. Robb, M. Olivucci, *Proc. Natl. Acad. Sci. USA* **2000**, *97*, 9379.
[44] W. Humphrey, H. Lu, I. Logonov, H. J. Werner, K. Schulten, *Biophys. J.* **1998**, *75*, 1689.
[45] S. Schenki, F. van Mourik, G. van der Zwan, S. Haacke, M. Chergui, *Science* **2005**, *309*, 917.
[46] J. Herbst, K. Heyne, R. Diller, *Science* **2002**, *297*, 822.
[47] G. Haran, K. Wynne, A. H. Xie, Q. He, M. Chance, R. M. Hochstrasser, *Chem. Phys. Lett.* **1996**, *261*, 389.
[48] F. Gai, K. C. Hasson, J. C. McDonald, P. A. Anfinrud, *Science* **1998**, *279*, 1886.
[49] J. Stuart, A. D. L. Mercy, K. Wise, *J. Synth. Metals.* **2002**, *127*, 3.
[50] L. Song, M. A. El-Sayed, *J. Am. Chem. Soc.* **1998**, *120*, 8889.
[51] M. Du, G. R. Fleming, *Biophys. Chem.* **1993**, *48*, 101.
[52] A. Kahan, O. Nahmias, N. Friedman, M. Sheves, S. Ruhman, S. *J. Am. Chem. Soc.* **2007**, *129*, 537.
[53] B.-X. Hou, N. Friedman, M. Ottolenghi, M. Sheves, S. Ruhman, *Chem. Phys. Lett.* **2003**, *381*, 549.
[54] A. C. Terentis, Y. D. Zhou, G. H. Atkinson, L. Ujj, *J. Phys. Chem. A* **2003**, *107*, 10787.
[55] M. Olivucci, A. Lami, F. Santoro, *Angew. Chem. Int. Ed.* **2005**, *44*, 5118.
[56] S. Hayashi, E. Tajkhorshid, K. Schulten, *Biophys. J.* **2003**, *85*, 1440.
[57] X. Chen, V. S. Batista, *J. Photochem. Photobiol. A* **2007**, *190*, 274.
[58] O. Weingart, *J. Am. Chem. Soc.* **2007**, *129*, 10618.
[59] B. Schobert, J. Cupp-Vickery, V. Hornak, S. O. Smith, J. K. Lanyi, *J. Mol. Biol.* **2002**, *321*, 715.
[60] Y. Matsui, K. Sakai, M. Murakami, Y. Shiro, S. Adachi, H. Okumura, T. Kouyama, *J. Mol. Biol.* **2002**, *324*, 469.
[61] M. Taiji, K. Bryl, M. Nakagawa, M. Tsuda, T. Kobayashi, *Photochem. Photobiol.* **1992**, *56*, 1003.
[62] J. Dobler, W. Zinth, K. Kaiser, D. Oesterhelt, *Chem. Phys. Lett.* **1988**, *144*, 215.
[63] K. C. Hasson, F. Gai, P. A. Anfinrud, *Proc. Natl. Acad. Sci. USA.* **1996**, *93*, 15124.
[64] L. Claisen, *Chem. Ber.* **1912**, *45*, 3157.
[65] F. E. Ziegler, *Chem. Rev.* **1988**, *88*, 1423.
[66] U. Nubbemeyer, *Synthesis*, **2003**, 961.
[67] A. M. M. Castro, *Chem. Rev.* **2004**, *104*, 2939.
[68] C. D. Hurd, M. A. Pollack, *J. Am. Chem. Soc.* **1938**, *60*, 1905.
[69] R. Hoffmann, R. B. Woodward, *Acc. Chem. Res.* **1968**, *1*, 17.
[70] K. Fukui, *Accts. Chem. Res.* **1971**, *4*, 57.
[71] W. v. E. Doering, W. R. Roth, *Tetrahedron* **1962**, *18*, 67.
[72] P. Vittorelli, T. Winkler, H. J. Hansen, H. Schmid, *Helv. Chim. Acta.* **1968**, *51*, 1457.
[73] H. J. Hansen, H. Schmid, *Tetrahedron* **1974**, *30*, **1959**.
[74] J. J. Gajewski, J. Jurayj, D. R. Kimbrough, M. E. Gande, B. Ganem, B. K. Carpenter, *J. Am. Chem. Soc.* **1987**, *109*, 1170.
[75] R. L. Vance, N. G. Rondan, K. N. Houk, F. Jensen, W. T. Borden, A. Komornicki, E. Wimmer, *J. Am. Chem. Soc.* **1988**, *110*, 2314.
[76] O. Wiest, K. A. Black, K. N. Houk, *J. Am. Chem. Soc.* **1994**, *116*, 10336.
[77] H. Hu, M. N. Kobrak, C. Xu, S. Hammes-Schiffer, *J. Phys. Chem. A* **2000**, *104*, 8058.
[78] J. G. Hill, P. B. Karadakov, D. L. Cooper, *Theor. Chem. Acc.* **2006**, *115*, 212.
[79] M. J. S. Dewar, E. F. Healy, *J. Am. Chem. Soc.* **1984**, *106*, 7127.
[80] M. J. S. Dewar, C. Jie, *J. Am. Chem. Soc.* **1989**, *111*, 511.
[81] J. J. Gajewski, N. D. Conrad, *J. Am. Chem. Soc.* **1979**, *101*, 2747.
[82] L. Kupczyk-Subotkowska, W. H. Saunders Jr., H. J. Shine, W. Subotkowski, *J. Am. Chem. Soc.* **1994**, *116*, 7088.
[83] M. M. Davidson, I. H. Hillier, *J. Phys. Chem.* **1995**, *99*, 6748.
[84] J. J. Gajewski, *Chem. Res.* **1997**, *30*, 219.
[85] V. Aviyente, H. Y. Yoo, K. N. Houk, *J. Org. Chem.* **1997**, *62*, 6121.
[86] H. Y. Yoo, K. N. Houk *J. Am. Chem. Soc.* **1997**, *119*, 2877.
[87] M. P. Meyer, A. J. DelMonte, D. A. Singleton, *J. Am. Chem. Soc.* **1999**, *121*, 10865.
[88] I. Iwakura, A. Yabushita, T. Kobayashi, *Chem. Lett.* **2010**, *39*, 374.

[89] I. Iwakura, A. Yabushita, T. Kobayashi, *J. Am. Chem. Soc.* **2009**, *131*, 688.
[90] M. J. J. Vrakking, D. M. Villeneuve, A. Stolow, *Phys. Rev. A* **1996**, *54*, R37.
[91] M. J. Frisch, G. W. Trucks, H. B. Schlegel, G. E. Scuseria, M. A. Robb, J. R. Cheeseman, J. A. Montgomery, Jr., T. Vreven, K. N. Kudin, J. C. Burant, J. M. Millam, S. S. Iyengar, J. Tomasi, V. Barone, B. Mennucci, M. Cossi, G. Scalmani, N. Rega, G. A. Petersson, H. Nakatsuji, M. Hada, M. Ehara, K. Toyota, R. Fukuda, J. Hasegawa, M. Ishida, T. Nakajima, Y. Honda, O. Kitao, H. Nakai, M. Klene, X. Li, J. E. Knox, H. P. Hratchian, J. B. Cross, V. Bakken, C. Adamo, J. Jaramillo, R. Gomperts, R. E. Stratmann, O. Yazyev, A. J. Austin, R. Cammi, C. Pomelli, J. W. Ochterski, P. Y. Ayala, K. Morokuma, G. A. Voth, P. Salvador, J. J. Dannenberg, V. G. Zakrzewski, S. Dapprich, A. D. Daniels, M. C. Strain, O. Farkas, D. K. Malick, A. D. Rabuck, K. Raghavachari, J. B. Foresman, J. V. Ortiz, Q. Cui, A. G. Baboul, S. Clifford, J. Cioslowski, B. B. Stefanov, G. Liu, A. Liashenko, P. Piskorz, I. Komaromi, R. L. Martin, D. J. Fox, T. Keith, M. A. Al-Laham, C. Y. Peng, A. Nanayakkara, M. Challacombe, P. M. W. Gill, B. Johnson, W. Chen, M. W. Wong, C. Gonzalez, J. A. Pople, Gaussian 03, Revision D.02, Gaussian, Inc., *Wallingford CT*. **2004**.
[92] T. Saito, T. Kobayashi, *J. Phys. Chem. A*, **2002**, *106*, 9436.
[93] T. Fuji, T. Saito, T. Kobayashi, *Chem. Phys. Lett.* **2000**, *332*, 324.
[94] A. Yabushita, T. Kobayashi, *Biophys. J.* **2009**, *96*, 1447.
[95] T. Kobayashi, A. Yabushita, *Chem. Phys. Lett.* **2009**, *482*, 143.
[96] I. Iwakura, A. Yabushita, T. Kobayashi, *Chem. Phys. Lett.* **2008**, *457*, 421.

